PAPER

Mesoporous Cu–Cu₂O@TiO₂ heterojunction photocatalysts derived from metal–organic frameworks†

Wenling Zhao and Chengcheng Liu [iD] *

This study reveals a unique Cu–Cu₂O@TiO₂ heterojunction photocatalyst obtained with metal–organic framework as the precursor, which can be utilized in dye photodegradation under visible light irradiation. The composition, structure, morphology, porosity, optical properties and photocatalytic performance of the obtained catalysts were all investigated in detail. The Cu–Cu₂O@TiO₂ nanocomposite is composed of lamellar Cu–Cu₂O microspheres embedded by numerous TiO₂ nanoparticles. Methylene blue, methyl orange and 4-nitrophenol were used as model pollutants to evaluate the photocatalytic activity of the Cu–Cu₂O@TiO₂ nanocomposite for dye degradation under visible light irradiation. Nearly 95% decolourisation efficiency of Methylene blue was achieved by the Cu–Cu₂O@TiO₂ photocatalyst within 3 h, which is much higher than that of TiO₂ or Cu₂O catalysts. The excellent photocatalytic activity was primarily attributed to the unique MOF-based mesoporous structure, the enlarged photo-adsorption range and the efficient separation of the charge carriers in the Cu–Cu₂O@TiO₂ heterojunction.

1. Introduction

Photocatalysis has emerged as an economical and environmentally benign reaction route and has shown potential in tackling resource depletion in recent years.[1,2] In this process, the light energy can be converted into the energy required for chemical reactions. Semiconductors, *e.g.*, TiO₂, Cu₂O, Cu₂₋ₓSe, and g-C₃N₄ *etc.*, with relatively low cost, high catalytic activity and stability are commonly used as photocatalysts.[3–6] Silver based nanocomposites are also photocatalysts for dye degradation.[7,8] Titanium dioxide (TiO₂), known as one of the most important n-type semiconductors, has been recognised as a photocatalyst owing to its own characteristics such as good photostability, low cost and environmental friendliness.[3,4] Due to its wide bandgap (anatase, 3.2 eV), TiO₂ can only be excited by ultraviolet light for photocatalytic reactions.[9] However, ultraviolet light only accounts for 5% of the solar spectrum, while visible light accounts for 48% of the total light energy.[10] At the same time, the photogenerated positive and negative charge carriers, electron–hole pairs, tend to recombine in single-phase semiconductors, resulting in the low efficiency of photocatalytic reactions. To overcome these shortcomings, a great number of efforts have been devoted to modifying the TiO₂ nanostructure surface or combining single-phase TiO₂ with non-metals,

metals, and organic molecules to form semiconductor composites. It has been reported that the combination of two or more desirable semiconductors or metal nanoparticles is an effective method to create nanocomposites with higher photocatalytic activity.[11,12] Because the photogenerated electrons are found to be transferable between them in a composite, which can significantly promote the separation of electron–hole pairs and finally improve photocatalytic efficiency. It is well known that narrow-bandgap semiconductor can serve as the primary absorber of visible light in a coupled semiconductor. Among narrow-bandgap semiconductors, Cu₂O is a naturally occurring p-type semiconductor with a wide range of applications such as photocatalytic water splitting, gas sensing, and degradation of organic pollutants.[13–15] Different from TiO₂, Cu₂O can be easily excited by visible light to generate electron and hole pairs on account of its lower bandgap energy (2.17 eV).[16] The matched band structures of Cu₂O and TiO₂ are sufficient to promote the physical separation of charge carriers, and also significantly inhibit the recombination rate in their nanocomposite, thereby increasing the light-harvesting efficiency and enhancing photocatalytic activity.[17] Moreover, the use of Cu coupled to Cu₂O and TiO₂ has shown better performance owing to the surface plasmon resonance (SPR) effect of Cu nanoparticles.[18,19] However, according to the literature, the synthesis of Cu–Cu₂O–TiO₂ nanocomposites requires sophisticated equipment, and it is very difficult to obtain a well-designed unique three-dimensional morphology of the nanocomposites. For this reason, the development of a controllable and straightforward synthetic route for Cu–Cu₂O–TiO₂ photocatalysts with novel

Institute of Molecular Sciences and Engineering, Institute of Frontier and Interdisciplinary Science, Shandong University, Qingdao 266237, P. R. China. E-mail: chengcheng.liu@sdu.edu.cn

structures and remarkable photocatalytic performance under visible light remains a challenge.
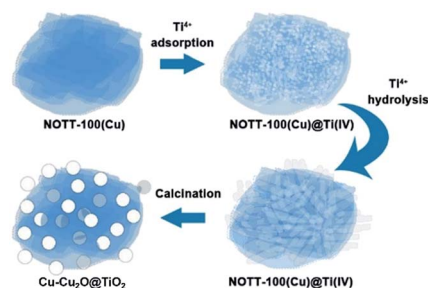
Catalysts with controlled porosity and morphology have shown great advantages in catalysis owing to their good mass transfer property, large surface area and abundant reactive sites.[20] Due to its unique porous structure and tuneable organic linkers/metal clusters, MOFs have attracted considerable attention as precursors to derive various useful porous catalytic materials by thermal or chemical treatments. For example, thermal treatment of MOFs in an inert atmosphere can produce highly porous carbon with a high specific surface area ($\sim$3000 $m^2 g^{-1}$).[21] Besides, direct heat treatment of MOF in the optimised heating conditions in a nitrogen or air atmosphere can lead them to decompose into their corresponding metal oxides.[22] In general, the derivative metal oxides have the same structure as the parent MOFs, and show much higher surface area than metal oxides produced by other methods. The high surface area, controllable porous architectures and tuneable composition of MOF-derived metal oxides along with the possibilities to combine them with different catalytic active metal oxides make them attractive candidates for the catalytic applications.[23] Over the years, metal-oxide semiconductors (MOS) have received the extensive concern on account of their high photo-response activity and nontoxicity in the application of solar energy conversion and environmental pollution reduction.[24]

Based on the above considerations, this work utilized cheap copper MOFs, NOTT-100 (Cu), as precursor to develop a kind of photocatalytic-active porous Cu–Cu_2O@TiO_2 triple junction nanocomposite, which was built by Cu–Cu_2O microspheres coated by a great many TiO_2 nanoparticles. To investigate the structure and morphology of Cu–Cu_2O@TiO_2 nanocomposite and its optical properties, XRD, SEM, UV-vis, *etc.* were conducted. The Cu–Cu_2O@TiO_2 shows good photocatalytic activity in organic pollutants degradation under visible-light illumination. The synergic effect endows the composite higher performance and the enhancement of the catalysis was attributed to the special heterojunction structure and the mesoporous structure.

2.   Results and discussion

2.1   Structure and morphology

In this project, Cu–Cu_2O@TiO_2 nanocomposite was synthesised by an easy two-step method. NOTT-100(Cu) lamellar microstructures were obtained firstly using the solvothermal method, and then tetra-*n*-butyl orthotitanate, the Ti(IV) precursors, were adsorbed on the porous surface of MOF microstructures, taking advantage of porosity of MOFs and strong hydrolysis ability of Ti(IV) precursors to produce the Cu–Cu_2O@TiO_2 nanocomposite after calcination (Scheme 1). Firstly, tetra-*n*-butyl orthotitanate was dissolved in the NOTT-100(Cu) suspension in *n*-hexane. Abundant Ti^{4+} cations would be diffused and adsorbed onto the surfaces of the porous NOTT-100(Cu) and partially hydrolysed with water molecules on the MOFs. After the separation of solvent *n*-hexane, Ti^{4+} cations further hydrolysed quickly with the moisture in the air. With the calcination, NOTT-100(Cu)

Scheme 1   Synthesis procedure of Cu–Cu_2O@TiO_2 nanocomposite.

totally decomposed to Cu_2O at 550 °C in 2 h. Then part of the Cu_2O decomposed to Cu when heated continuously to 4 h (Fig. S2†). Hence Cu_2O and Cu coexist under the adopted calcination temperature and time conditions. Besides, a large number of TiO_2 nanoparticles were formed from hydrolysed products, obtaining TiO_2 nanoparticles grown on Cu–Cu_2O microspheres.

This adsorption and hydrolysis procedure did not influence the unique structure of NOTT-100(Cu) as shown in Fig. S1.† The calcination temperature of 550 °C and duration of 4 hours are selected as the optimised calcination condition for Cu–Cu_2O formation without CuO (Fig. S2†). For this sample, all diffraction peaks in the XRD pattern are almost consistent with each value of the standard patterns of anatase phase TiO_2 (JCPDS card no. 21-1272), Cu (JCPDS card no. 04-0836) and Cu_2O (JCPDS card no. 05-0667), indicating the good-crystalline character of the samples.

In Fig. 1, SEM and TEM images illustrate the morphologies and microstructures of NOTT-100(Cu) and Cu–Cu_2O@TiO_2, respectively. It can be clearly seen that the Cu–Cu_2O@TiO_2 nanocomposite consists of flower-like lamellar microspheres with a diameter of about 2.5 μm keeping the primary structure of NOTT-100(Cu), and a large number of nanoparticles covered on the surface of lamellar microstructures. In addition, Fig. 1e shows the HRTEM image of the Cu–Cu_2O@TiO_2, from which it can be seen that the lattice space of 0.366 nm corresponds to (116) planes of TiO_2. The lattice space of 0.241 nm corresponds
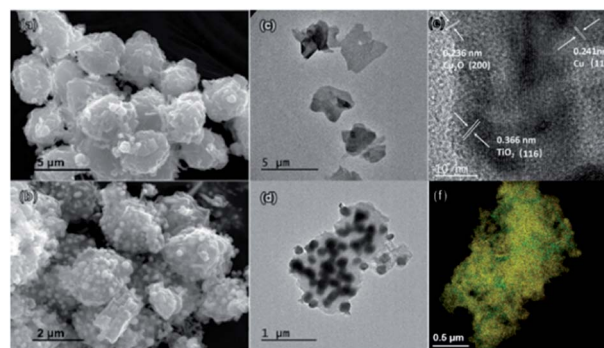

Fig. 1   SEM and TEM images of the NOTT-100(Cu) (a) and (c); Cu–Cu_2O@TiO_2 (b) and (d). HRTEM images of the Cu–Cu_2O@TiO_2 (e). EDS mapping of O (red), Ti (green) and Cu (yellow) in Cu–Cu_2O@TiO_2 (f).

to (111) planes of Cu, and the lattice space of 0.236 nm corresponds to (200) planes of Cu_2O. EDS mapping shows the element distribution of O, Ti and Cu in $Cu–Cu_2O@TiO_2$ (Fig. 1f and S3†). These characterizations demonstrate that almost all TiO_2 nanoparticles attached to the $Cu–Cu_2O$ surface are separately and evenly distributed. Hence, it can be concluded that the as-prepared rough $Cu–Cu_2O@TiO_2$ nanocomposite is composed of the MOF-like lamellar $Cu–Cu_2O$ microspheres embedded by a great many TiO_2 nanoparticles.

The porosity of the $Cu–Cu_2O@TiO_2$ sample was investigated by N_2 adsorption–desorption isotherm patterns (Fig. S4†). The isotherm is similar to type-IV IUPAC isotherm which indicates the $Cu–Cu_2O@TiO_2$ sample is a kind of mesoporous material. The average pore diameter is determined about 7 nm. It is reported that mesoporous structure has a large specific surface area, providing a large number of active centers for the reaction. Moreover, the existence of mesoporous structure is conducive to multiple light scattering or reflection, thus enhancing the capture of exciting light and improving the photocatalytic activity.[25–27] The BET surface area and the pore volume of $Cu–Cu_2O@TiO_2$ are 187 $m^2 g^{-1}$ and 0.298 $cm^3 g^{-1}$ respectively. The BET surface is much higher than the reported $Cu–Cu_2O–TiO_2$ composite ($50 m^2 g^{-1}$) owing to the porous properties.[28] The mesopores are assumed to result from the loss of organic ligands in MOF during calcination. Therefore, the $Cu–Cu_2O@TiO_2$ nanocomposite is revealed to have an excellent porous property, which can be another advantage for the catalytic application.

2.2 XPS analysis

XPS studies were conducted over the $Cu–Cu_2O@TiO_2$ in order to understand the chemical state and chemical environment of the Cu and Ti elements of the composite. Fig. 2a shows the XPS survey spectrum for $Cu–Cu_2O@TiO_2$ composites, which demonstrates the existence of Cu, Ti, O and C elements in the sample. The spectra were calibrated with C 1s as standard. Fig. 2b shows the high resolution XPS spectrum in the region of

Cu 2p for $Cu–Cu_2O@TiO_2$. The main peak centered at 932.4 and 952.4 eV of Cu $(2p_{3/2})$ and Cu $(2p_{1/2})$ are readily assigned to either Cu(0) or Cu(ı). The two binding energy peaks located at 934.1 and 954.0 eV with two extra shake-up satellites were assigned to Cu $(2p_{3/2})$ and Cu $(2p_{1/2})$ of Cu(ıı).[29] This was commonly attributed to the oxidation of Cu(ı) during sample preparation for analysis as there is no CuO shown in the XRD spectrum.[30] The high resolution XPS spectrum of Ti 2p in $Cu–Cu_2O@TiO_2$ (Fig. 2c) centered in 458.3 and 464.0 eV can be assigned to Ti $(2p_{3/2})$ and Ti $(2p_{1/2})$ for Ti(ıv).[31]

2.3 Optical properties and photocatalytic performance

The UV-vis diffuse reflectance spectroscopy was employed to investigate the optical properties of the $Cu–Cu_2O@TiO_2$ sample. The UV-vis absorption spectra of pure $Cu–Cu_2O@TiO_2$ nanocomposite, pure commercially available TiO_2 (anatase) nanoparticles, pure NOTT-100(Cu) are shown in Fig. 3a. It can be clearly seen that the pure TiO_2 presents strong absorption of ultraviolet light at wavelengths below 400 nm. As desired, the $Cu–Cu_2O@TiO_2$ nanocomposite exhibits much stronger absorption, especially in wavelengths ranging from 400 to 600 nm, which could be attributed to the interplay of Cu_2O and TiO_2 and the narrow band-gap of Cu_2O.

Using the Tauc plot of $(Ah\nu)^2$ versus photon energy $(h\nu)$, the optical bandgap of the direct allowed semiconductor could be roughly determined.[32] As shown in Fig. 3b, the measured bandgap of pure TiO_2 and pure NOTT-100(Cu) is about 3.34 eV and 3.67 eV, respectively. As the coupling of $Cu–Cu_2O$ has a significant effect on the band-gap energy of TiO_2, the estimated band-gap of the $Cu–Cu_2O@TiO_2$ nanocomposite is 2.25 eV, which is much lower than band-gap of either pure TiO_2 or pure NOTT-100(Cu) but little higher than that of reported pure Cu_2O (2.17 eV).[33] These results indicate that the interfaces of $Cu–Cu_2O$ and TiO_2 are combined intimately, and the band edges achieve good matching between the two semiconductors.

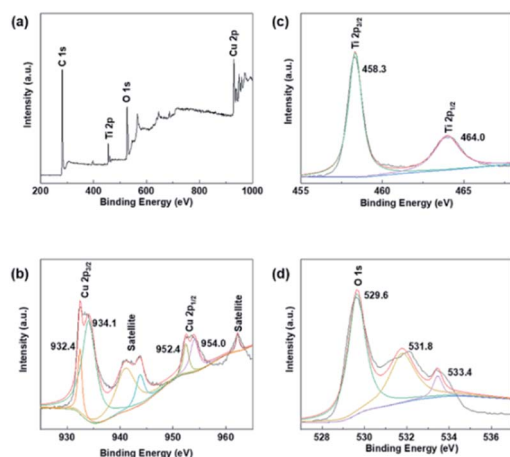**Fig. 2** XPS spectra of $Cu–Cu_2O@TiO_2$: (a) XPS survey spectrum, (b) Cu 2p spectrum, (c) Ti 2p spectrum and (d) O 1s spectrum.

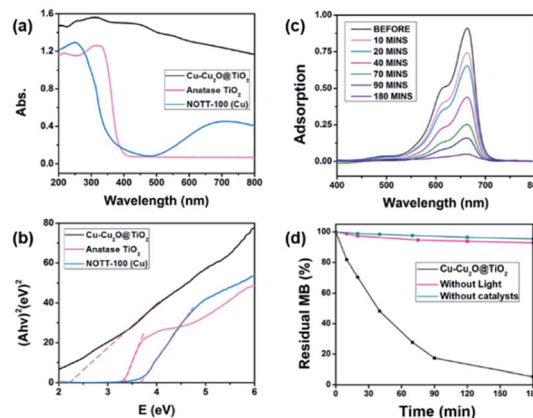**Fig. 3** (a) UV-vis diffuse-reflectance spectra and (b) Tauc plots of $(Ah\nu)^2$ versus $(h\nu)$ of $Cu–Cu_2O@TiO_2$, TiO_2(anatase) and NOTT-100(Cu), respectively; (c) UV-vis absorption spectra for MB solution in the presence of $Cu–Cu_2O@TiO_2$ nanocomposite under the visible light irradiation at different time intervals; (d) MB residual under different conditions.

Hence, the visible light harvest and high-efficient separation of electron and hole pairs are more likely to accomplish in the Cu–Cu$_2$O@TiO$_2$ nanocomposite.

In this work, methylene blue (MB), methyl orange (MO) and 4-nitrophenol (4-NP) were utilised as model pollutants to investigate the photocatalytic activity of Cu–Cu$_2$O@TiO$_2$ nanocomposite under the visible light irradiation. Fig. 3c exhibits the UV-vis absorption spectrum of the MB aqueous solution with 5 mg of Cu–Cu$_2$O@TiO$_2$ as photocatalyst exposed to the visible light for different durations. And it is observed that the characteristic absorption peak of MB at 664 nm becomes weaker rapidly when the exposure time is extended. After about 180 minutes, the peak almost disappears. Meanwhile, the MB aqueous solution turned colourless gradually from beginning blue under the irradiation. This degradation efficiency of MB is much higher than that of the reported Cu$_2$O@TiO$_2$ composite or Cu–TiO$_2$/RGO catalysts.[34,35]

Blank tests (without any catalysts or without light) were completed which exhibit a slight fall of the MB concentration (Fig. 3d). The results of the MB photodegradation with different photocatalysts under the same conditions are compared in Fig. S5.† After 180 minutes of the visible-light irradiation, about 12%, 11% and 30% of MB are decomposed catalysed by the pure commercial anatase nanoparticles, NOTT-100(Cu) and Cu$_2$O obtained from the calcination of NOTT-100(Cu), respectively. These results also suggest that the Cu–Cu$_2$O@TiO$_2$ nanocomposite has a much more excellent photocatalytic activity, compared to either pure TiO$_2$, Cu$_2$O or NOTT-100(Cu) under the visible light irradiation (Table S1†). To further explore the practical applications of the Cu–Cu$_2$O@TiO$_2$ photocatalyst, the repeatability test was completed by recycling the sample three times in the degradation of MB under the same condition. In Fig. S6,† MB is found to be almost degraded entirely in each cycle, which suggests that there is no apparent decrease in photocatalytic activity in the three cycles. This result indicates that the Cu–Cu$_2$O@TiO$_2$ nanocomposite possesses good cycling stability for the photodegradation of MB.

When it was applied to the photodegradation of MO and 4-NP, Cu–Cu$_2$O@TiO$_2$ also shows good activity compared with pure TiO$_2$ and NOTT-100(Cu). It is found that the characteristic absorptions of MO at 464 nm (Fig. S7†) decrease under the visible light irradiation. As shown in Fig. S8,† after irradiation for 3 h, residual MO and 4-NP drop to 38% and 62%, respectively.

There are many reasons for this excellent photocatalytic performance of the Cu–Cu$_2$O@TiO$_2$ nanocomposite, and the most crucial one can be ascribed to the efficient separation of the charge carriers at the closely combined Cu–Cu$_2$O@TiO$_2$ heterojunctions. Pure TiO$_2$ nanoparticles can only be activated by ultraviolet light, whereas for Cu–Cu$_2$O@TiO$_2$ nanocomposite the photo-response range is widely extended. Therefore much more energy from the visible light can be utilised under the natural light irradiation. Moreover, the efficient separations of the photogenerated electron–hole pairs are driven by the heterojunction of p-type Cu$_2$O and n-type TiO$_2$ semiconductor. Although the TiO$_2$ nanoparticles cannot be excited by the visible light, Cu$_2$O can act as the primary absorber of visible light and

be activated to generate electron–hole pairs. As shown in Scheme 2, the position of the conduction band (CB) in Cu$_2$O is higher than that of TiO$_2$, and so the active electrons (e$^-$) in the CB of Cu$_2$O tend to transfer to the CB of TiO$_2$ when irradiated by the visible light. The photo-generated holes can effectively migrated to and accumulated at Cu$_2$O, and meanwhile this will promote the acceleration of the photogenerated electron–hole separation in Cu$_2$O and also curb the recombination of electron–hole pairs. In addition, the SPR electrons of Cu have enough energy to overcome the Schottky barrier formed on the Cu/Cu$_2$O interfaces, thus the SPR effect of Cu excited by the visible light also enable the electrons transfer to the Cu$_2$O.[36,37] In the catalytic process, the excited electrons would migrate to the catalyst surface where they could be trapped by the absorbed oxygen, thereby generating $\cdot$O^{2-} radicals. Then the oxidative H$_2$O$_2$ and $\cdot$OH radicals can be produced by the reaction of those $\cdot$O^{2-} radicals and H$^+$. Finally, the organic pollutant molecules are oxidised and degraded by these strong oxidative radicals.[38] Moreover, the porosity of the Cu–Cu$_2$O@TiO$_2$ nanocomposite should not be ignored as the high surface area can lead to better catalytic performance. Therefore, the Cu–Cu$_2$O@TiO$_2$ nanocomposite exhibits a remarkable photocatalytic performance under the visible light irradiation.
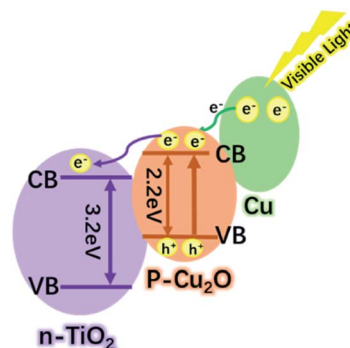
3. Experimental section

3.1 Materials and methods

XRD patterns were recorded on a Philip X'Pert with Cu-Kα radiation ($\lambda = 0.154184$ nm) at 40 kV and 50 mA with a scanning rate of 5° min^{-1}. Scanning electron microscopy (SEM) was performed on FEI XL30 ESEM-FEG. Ultraviolet-visible (UV-vis) diffuse-reflectance spectra were analysed at room temperature by UV-2600 (Shimadzu, Japan) with BaSO$_4$ and DI water as the references, which were converted to absorption spectra using the Kubelka–Munk method. Nuclear magnetic resonance (NMR) was recorded on Bruker Ascend TM 400; infrared spectroscopy (IR) was carried on ATR.

3.2 Synthetic procedures

3.2.1 General procedure for synthesis of NOTT-100(Cu).
The solvothermal method was used for the synthesis of

Scheme 2 Photocatalytic mechanism of Cu–Cu$_2$O@TiO$_2$ nanocomposite under visible light irradiation.

$[Cu_2(C_{16}H_6O_8)(H_2O)_2] \cdot 2.5$ DMF$\cdot 4H_2O$. Firstly, a quantity of 400 mg of H_4BPTC (1.21 mmol) and 832 mg of $Cu(NO_3)_2 \cdot 2.5H_2O$ (3.58 mmol) were mixed and dispersed in DMF/ethanol/H_2O (128 mL, 3 : 3 : 2 v/v/v) in a 250 mL round-bottom flask. Then CTAB (9.6 g, 26.34 mmol) was added to the mixture and mixed thoroughly. The suspension was heated with continuous stirring in a 65 °C oil bath for 24 hours, and a large amount of microcrystalline product precipitated. The blue crystalline product was washed with warm DMF (65 °C), H_2O and acetone in turn, and dried briefly in the air. Yield: 745 mg (82.8%).

3.2.2 Synthesis of NOTT-100@Ti(IV). A quantity of 60 mg of NOTT-100(Cu) (807 μmol) was dispersed in 10 mL of *n*-hexane in a small glass vial with lid firstly. Then tetra-*n*-butyl orthotitanate (120 μL, 349 μmol) was dropwise added to the mixture and covered with lid rapidly. The suspension was continuously stirred for 24 hours. Finally, the blue product was separated by centrifugation at 8000 rpm for 2 min and dried briefly in the air.

3.2.3 Synthesis of Cu–Cu$_2$O@TiO$_2$. A quantity of 60 mg of NOTT-100@Ti(VI) was placed in a small porcelain boat packing with tin foil paper, and then calcined at 550 °C for 4 hours (heating rate: 5 °C min^{-1}) in the tube furnace. After calcination, the blue material turned into dark brown. Yield: 14 mg (23.3%). Elemental analysis: $Cu_8TiO_{5.8}$ (Cu, 78.47; Ti, 7.37%).

3.3 Photocatalytic experiments

The model organic pollutant, MB, was utilised to investigate the photocatalytic performance of samples under visible-light illumination. First, a quantity of 5 mg of the synthesised Cu–Cu$_2$O@TiO$_2$ was dispersed in 12.5 mL of deionised water (DI) (0.4 mg mL^{-1}) *via* ultrasonication for 1 minute in a 60 mL glass beaker, and then 12.5 mL of a 4×10^{-5} M MB aqueous solution was added. A 300 W xenon lamp (CEL- HXF300, Beijing Aulight Co., Ltd., Beijing, PRC) served as the light source, equipped with a 400 nm cut-off glass sheet to filter out all the light at wavelengths below 400 nm. At the same time, the photocatalytic reactor and the visible light source was shielded by black cardboards during the reaction to remove the interference from outside light. Before illuminated by the visible light, the mixed solution of the photocatalyst and MB was under continuous magnetic stirring in darkness for 1 hour to establish an adsorption–desorption equilibrium. The suspension was also stirred during the whole irradiation process. At each time interval, 2 mL of the reaction liquid was taken out by a clean syringe, and the photocatalyst was removed by centrifugation at 10 000 rpm for 2 minutes. Then the clear MB solution was analysed by the Model UV-2600 spectrophotometer, with the measured maximum absorption at $\lambda_{max} = 664$ nm. NOTT-100(Cu), NOTT-100(Cu)@Ti(IV), TiO$_2$ anatase nanoparticles, Cu$_2$O after calcination of NOTT-100(Cu) were also applied into the degradation experiments of MB under the same experimental conditions for comparison purpose. For the degradation of MO and 4-NP, the experimental conditions are similar with MB, but with different initial concentrations. For MO, the concentrations of MO and the photocatalyst are 30 mg L^{-1} and 0.25 mg mL^{-1}, respectively. For 4-NP, the fixed initial concentrations of 4-NP and the photocatalyst in the solution were 10 mg L^{-1} and 0.36 mg mL^{-1}, respectively. All the photocatalytic degradation experiments were repeated three times.

4. Conclusions

In summary, the Cu–Cu$_2$O@TiO$_2$ mesoporous nanocomposite was successfully obtained by a facile two-step route, and its application in the photocatalytic degradation of organic pollutants under the visible light irradiation was utterly investigated. The Cu–Cu$_2$O@TiO$_2$ nanocomposite presents a lamellar Cu–Cu$_2$O microsphere, embedded by numerous TiO$_2$ nanoparticles. In the photodegradation of MB with the Cu–Cu$_2$O@TiO$_2$ nanocomposite, nearly 100% decolorization efficiency was achieved under the visible light in 3 h. The excellent photocatalytic property of the Cu–Cu$_2$O@TiO$_2$ nanocomposite can be ascribed to the unique mesoporous structure constructed from MOFs, the enlarged photo-adsorption range and also the efficient separation of the electron–hole pairs in its heterojunction. These characteristics indicate the Cu–Cu$_2$O@TiO$_2$ nanocomposite has huge potential for photodegradation of organic pollutants from water and the other environmental discharge.

Conflicts of interest

There are no conflicts to declare.

Acknowledgements

References

1 M. D. Karkas, B. S. Matsuura and C. R. J. Stephenson, *Science*, 2015, **349**, 1285.

2 H. H. Huo, X. D. Shen, C. Y. Wang, L. L. Zhang, P. Rose, L. A. Chen, K. Harms, M. Marsch, G. Hilt and E. Meggers, *Nature*, 2014, **515**, 100.

3 A. Fujishima and K. Honda, *Nature*, 1972, **238**, 37.

4 M. R. Hoffmann, S. T. Martin, W. Choi and D. W. Bahnemann, *Chem. Rev.*, 1995, **95**, 69.

5 W. W. Zhong, S. J. Shen, S. S. Feng, Z. P. Lin, Z. P. Wang and B. Z. Fang, *CrystEngComm*, 2018, **20**, 7851.

6 G. Liao, Y. Gong, L. Zhang, H. Gao, G. J. Yang and B. Fang, *Energy Environ. Sci.*, 2019, **12**, 2080.

7 G. F. Liao, J. S. Fang, Q. Li, S. H. Li, Z. S. Xu and B. Z. Fang, *Nanoscale*, 2019, **11**, 7062.

8 G. F. Liao, Y. Gong, L. Zhong, J. S. Fang, L. Zhang, Z. S. Xu, H. Y. Gao and B. Z. Fang, *Nano Res.*, 2019, **12**, 2407.

9 H. X. Li, Z. F. Bian, J. Zhu, D. Q. Zhang, G. S. Li, Y. N. Huo, H. Li and Y. F. Lu, *J. Am. Chem. Soc.*, 2007, **129**, 4538.

10 H. Xu, S. X. Ouyang, L. Q. Liu, P. Reunchan, N. Umezawa and J. H. Ye, *J. Mater. Chem. A*, 2014, **2**, 12642.

11 Y. Y. Li, L. Y. Dang, L. F. Han, P. P. Li, J. S. Wang and Z. J. Li, *J. Mol. Catal. A: Chem.*, 2013, **379**, 146.

12 D. H. Xiong, H. M. Chang, Q. Q. Zhang, S. Q. Tian, B. S. Liu and X. J. Zhao, *Appl. Surf. Sci.*, 2015, **347**, 747.

13 L. I. Hung, C. K. Tsung, W. Y. Huang and P. D. Yang, *Adv. Mater.*, 2010, **22**, 1910.

14 W. C. Huang, L. M. Lyu, Y. C. Yang and M. H. Huang, *J. Am. Chem. Soc.*, 2012, **134**, 1261.

15 C. H. Kuo and M. H. Huang, *J. Am. Chem. Soc.*, 2008, **130**, 12815.

16 Q. Yang, M. Long, L. Tan, Y. Zhang, J. Ouyang, P. Liu and A. D. Tang, *ACS Appl. Mater. Interfaces*, 2015, **7**, 12719.

17 Y. F. Wang, J. J. Tao, X. Z. Wang, M. Zhang, G. He and Z. Q. Sun, *Ceram. Int.*, 2017, **43**, 4866.

18 J. Xing, Z. P. Chen, F. Y. Xiao, X. Y. Ma, C. Z. Wen, Z. Li and H. G. Yang, *Chem.–Asian J.*, 2013, **8**, 1265.

19 L. Rekeb, L. Hamadou, A. Kadri, N. Benbrahim and E. Chainet, *Int. J. Hydrogen Energy*, 2019, **44**, 10541.

20 C. C. Liu, J. L. Zhang, L. Peng, X. C. Kang, B. X. Han, X. X. Sang, X. Ma and G. Y. Yang, *Microporous Mesoporous Mater.*, 2015, **217**, 6.

21 P. Pachfule, X. C. Yang, Q. L. Zhu, N. Tsumori, T. Uchida and Q. Xu, *J. Mater. Chem. A*, 2017, **5**, 4835.

22 C. Young, J. Kim, Y. V. Kaneti and Y. Yamauchi, *ACS Appl. Energy Mater.*, 2018, **1**, 2007.

23 Y. V. Kaneti, J. Tang, R. R. Salunkhe, X. Jiang, A. Yu, K. C.-W. Wu and Y. Yamauchi, *Adv. Mater.*, 2017, **29**, 1604898.

24 X. Q. Liu, J. Iocozzia, Y. Wang, X. Cui, Y. H. Chen, S. Q. Zhao, Z. Li and Z. Q. Lin, *Energy Environ. Sci.*, 2017, **10**, 402.

25 B. Z. Fang, M. Kim, S. Q. Fan, J. H. Kim, D. P. Wilkinson, J. Ko and J. S. Yu, *J. Mater. Chem.*, 2011, **21**, 8742.

26 B. Z. Fang, Y. L. Xing, A. Bonakdarpour, S. C. Zhang and D. P. Wilkinson, *ACS Sustainable Chem. Eng.*, 2015, **3**, 2381.

27 B. Z. Fang, A. Bonakdarpour, K. Reilly, Y. L. Xing, F. Taghipour and D. P. Wilkinson, *ACS Appl. Mater. Interfaces*, 2014, **6**, 15488–15498.

28 X. Q. An, H. J. Liu, J. H. Qu, S. J. A. Moniz and J. W. Tang, *New J. Chem.*, 2015, **39**, 314.

29 Q. Huang, F. Kang, H. Liu, Q. Li and X. D. Xiao, *J. Mater. Chem. A*, 2013, **1**, 2418.

30 M. E. Aguirre, R. X. Zhou, A. J. Eugene, M. I. Guzman and M. A. Grela, *Appl. Catal., B*, 2017, **217**, 485.

31 M. Logar, I. Bracko, A. Potocnik and B. Jancar, *Langmuir*, 2014, **30**, 4852.

32 J. Tauc, *Mater. Res. Bull.*, 1968, **3**, 37.

33 Z. Q. Jiang, G. Yao, X. Y. An, Y. J. Fu, L. H. Cao, W. D. Wu and X. M. Wang, *Chin. Phys. B*, 2014, **23**, 1674.

34 L. M. Liu, W. Y. Yang, W. Z. Sun, Q. Li and J. K. Shang, *ACS Appl. Mater. Interfaces*, 2015, **7**, 1465.

35 T. T. Pham, N. H. Chinh, H. J. Lee, T. D. Nguyen-Phan, T. H. Son, C. K. Kim and E. W. Shin, *Ceram. Int.*, 2015, **41**, 11184.

36 Y. V. Kaneti, J. Tang, R. R. Salunkhe, X. C. Jiang, A. B. Yu, K. C. W. Wu and Y. Yamauchi, *Adv. Mater.*, 2017, **29**, 1604898.

37 L. Rekeb, L. Hamadou, A. Kadri, N. Benbrahim and E. Chainet, *Int. J. Hydrogen Energy*, 2019, **44**, 10541.

38 F. A. Qaraah, S. A. Mahyoub, M. E. Hafez and G. L. Xiu, *RSC Adv.*, 2019, **9**, 39561.